Tunable ground state in heterostructured artificial spin ice with exchange bias

Vineeth Mohanan Parakkat, Kaichen Xie, and Kannan M. Krishnan

Phys. Rev. B **99**, 054429 — Published 26 February 2019

DOI: 10.1103/PhysRevB.99.054429

Tunable ground state in heterostructured artificial spin ice with exchange bias

Vineeth Mohanan Parakkat, Kaichen Xie and Kannan M. Krishnan
Department of Materials Science and Engineering
323 Roberts Hall, University of Washington, Seattle, WA 98195, USA
e-mail address:kannanmk @uw.edu

We describe a new artificial spin ice (ASI) composed of exchange biased heterostructured nanomagnetic elements with unidirectional anisotropy and compare it with a conventional ASI constituted by ferromagnets with uniaxial anisotropy (Ising spins). The introduction of a local exchange bias field, aligned along one of the sublattices of the square ASI, lifts the spin reversal symmetry of the vertices. By varying the lattice constant of the square array, we control the ratio of exchange bias to dipolar field (H_{EB}/H_{dip}) and tune the ground state from an antiferromagnetic to a ferromagnetic configuration with an effective magnetic moment. The geometric frustration of dipolar interactions is moderated by a non-frustrated local field, leading to a mesoscopic system with specific metastable states observed during the demagnetization process.

Artificial spin ice (ASI) arrays are assemblies of nanomagnets interacting magnetostatically but are frustrated due to the geometry [1–3]. Although the ASI configuration was introduced [1] to mimic the physics of geometric frustration in spin ice pyrochlore materials [4,5], it rapidly evolved into novel areas of research pertaining to studies of vertex models [6–8], frustrated interactions [4,9–11], and a playground for studying emergent phenomenon in artificially engineered many body magnetic systems [1,12–15]. Taking advantage of the anisotropic nature of magnetostatic interactions and the possibility of lithographically engineering newer geometries, this area of research is only limited by one's imagination [16–18]. The first ASI system investigated, involving nanomagnets forming the edges of a square lattice, was initially found to be topologically identical to the spin ice system [19]. Later, it was identified to possess a *unique* ground state due to difference in interaction strengths of perpendicularly and collinearly aligned moments at the vertices, and unlike spin ice, it is not a truly geometrically frustrated system [20]. However, the true degeneracy of a square ASI was recovered by vertically shifting selective sublattices of a planar square tile array [21] such that the interaction strengths of all moments at the vertices are made equal. In general, studies of ASI (particularly, square and kagome geometries [22,23]) have mainly dealt with identifying their ground states [1], effective thermodynamics [24–26] and high energy excitations [13,27]. Further, most nanomagnets constituting ASI were fabricated of permalloy thin films with blocking temperatures well above room temperature. Hence, the ASI were highly athermal [25] making it impossible to observe thermally excited dynamics at room temperatures, and instead, a sample rotating demagnetization process was employed to drive them towards the lowest energy states [28–30]. Later studies investigated thermally driven dynamics in ASI (square lattice and kagome) by using materials with low blocking temperature [31] which allowed the ASI to explore the configurational phase space better than in demagnetization process [32,33] and hence achieving/reaching near ground state configurations [34–36]. In addition, most of the previous studies on ASI utilized single domain

ferromagnetic nanoelements that behave as giant Ising spins possessing uniaxial anisotropy and emphasized newer lattice geometries, such as brickwork [37], shakti [38], tetris [12], including topological defects [18] and even quasicrystal patterns [17], that can lead to frustration where the energetics are controlled by the vertex geometry and spin topology.

In this letter we investigate a new type of interacting nanomagnetic ASI system where the uniaxial ferromagnetic elements are replaced by *heterostructured* ones with exchange biased unidirectional anisotropy [39–45]. Even though the underlying geometry of the square ASI is retained, the *local* exchange coupling of the ferromagnet with an antiferromagnet within each heterostructured element lifts the spin reversal symmetry of one of the sublattices with easy axis parallel to the exchange bias direction. As a result, previously unreported magnetic configurations, after demagnetization by the standard sample rotation protocol, were observed. The square tile array of exchange biased epitaxially grown Fe/IrMn bilayers (EB-ASI) is fabricated and compared with a conventional square ASI fabricated of Fe films grown epitaxially on MgO substrates. Further, by fabricating arrays with different lattice spacing the nearest neighbor dipolar field, H_{dip}, between the heterostructured nanomagnets (with exchange bias H_{EB} = 60 Oe in the unpatterned bilayer film) is controlled such that H_{EB}/H_{dip} ratio varies from 0.97 to ~30 (an estimate of H_{dip} is made using micromagnetic simulations; details are in supplementary data). As H_{EB}/H_{dip} is varied, a rearrangement of the energies of the 16 different types of vertices, each with a unique configuration of moments (Fig. 1), based on their spin topology, occurs and affects the population statistics of vertex types. In a conventional square ASI, only the dipolar coupling contributes towards the assignment of energies of vertices, and results in 4 types of vertices namely T1, T2, T3 and T4 (in the order of increasing energies, with degeneracy of 2, 4, 8 and 2, respectively) (Fig. 1), where the spin topology is synonymous with the energy. In contrast, in EB-ASI, the local exchange bias field within the heterostructured elements of the array, results in the rearrangement of vertices categorized by energy and not by their spin topology alone. Hence, as we show below, the ground state of the EB-ASI can be tuned by varying the lattice spacing (i.e. controlling the ratio H_{EB}/H_{dip}). With the exchange bias along one of the sublattice directions [x-axis of device frame, Fig. 2(b)] the vertex configurations with spin topology resulting in an effective moment of the vertex parallel to the local field, become the ground state as elaborated in Figs. 1 & 4. Unlike the thermally driven ASI under an external field [46], the EB-ASI has built in exchange bias, equivalent to a permanent local field, which provides stable magnetic configurations at room temperatures for MFM imaging. Here, both the ASI and the EB-ASI are athermal since the energy barriers involved in reversing the magnetization orientation is very large compared to the thermal energies at room temperature and hence has negligible effect on their magnetization reversal. Thus, to drive the ASI devices towards their ground state at room temperature, they are subjected to a standard [28] rotating sample demagnetization protocol. The EB-ASI is robust, well-behaved, and shows reproducible ground state configurations as H_{EB}/H_{dip} is systematically varied by changing the lattice spacing of the square ASI. A clear cross-over from a T1-dominated to a T2-dominated ground state is observed with appearance of large densities of charged excitations T3 with an effective magnetic moment along the direction of exchange bias. In other words, a transition from an antiferromagnetic to ferromagnetic configuration with a net moment, is observed as H_{EB}/H_{dip} is increased.

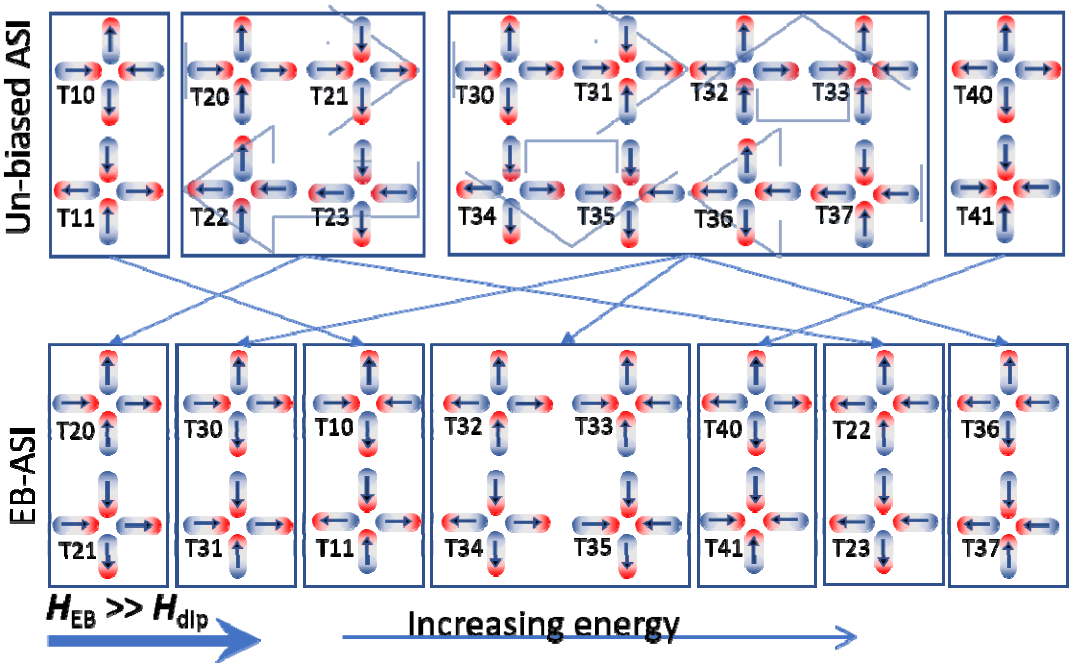

FIG. 1 Schematic representation of the energy levels of vertices for a normal ASI. The vertices are enumerated as (T10, T11), (T20, T21, T22, T23), (T30, T31, T32, T33, T34, T35, T36, T37) and (T40, T41). (top) The four possible types of vertices are (1) the ground state, T1 (two spins out, two spins in, no net moment), which is two-fold degenerate, with the two states related by a global spin-flip. (2) A saturated state, T2 (two spins out, two spins in, with net moment), with four-fold degeneracy, and where spins have a net projection parallel or antiparallel to the x-axis. (3) An eight-fold degenerate configuration, T3 (one spin in, three spins out, or, one spin out and three spins in, with moment along the x- or y-direction), and (4) a two-fold degenerate, T4 (all four spins in or all four spins out). (bottom) In the exchange biased ASI the vertices are energetically rearranged and represented here based on micromagnetic simulations. The 4-level system rearranges into a 7-level system. The dipolar vertices, with effective magnetic moments parallel to the bias direction are now lower in energy, with (T20, T21) being the ground state and (T10, T11) now excited even above the (T30, T31) states. Further, these energy levels can be tuned by the ratio H_{EB}/H_{dip} as described in the text.

The square ASI is fabricated from epitaxially grown thin films of Fe and Fe/IrMn on MgO substrates. First, epitaxial films of Fe (thickness of 10 nm) and exchange biased Fe (10 nm)/IrMn (8 nm) bilayers are grown at 280 °C on MgO (100) substrates by Ar ion-beam sputtering in a high vacuum chamber maintained at a base pressure of $5\text{x}10^{-8}$ Torr. The Fe/IrMn films are grown under an *in situ* magnetic field of ~ 200 Oe applied along the $\text{Fe}_{<100>}$ film (thus exchange bias direction $H_{EB}||\text{Fe}_{<100>} \parallel \text{MgO}_{<110>}$) [45]. A 2 nm thick Pt layer is deposited as a capping layer to prevent oxidation of Fe and Fe/IrMn bilayers. The in-plane hysteresis of Fe/IrMn films measured using longitudinal MOKE indicated an exchange bias H_{EB} ~ 60 Oe [Fig. 2(a)]. The ASI array is fabricated using a hard mask transfer technique and Ar ion milling process. The sacrificial mask of Mo layers is prepared by electron beam lithography, sputtering and lift-off, and after the milling process, any Mo mask residue is chemically removed using

H_2O_2 solution. During the patterning process the edge of the square ASI is aligned with $Fe_{<100>}$, which is also the exchange bias direction of the Fe/IrMn films as indicated in Fig. 2(b). The fabricated nanomagnets had a lateral dimension of 90 nm x 240 nm, corresponding to each element being a single magnetic domain, as confirmed by MFM imaging over thousands of nanomagnets and the total fabricated area of each array is 40 μm x 40 μm.

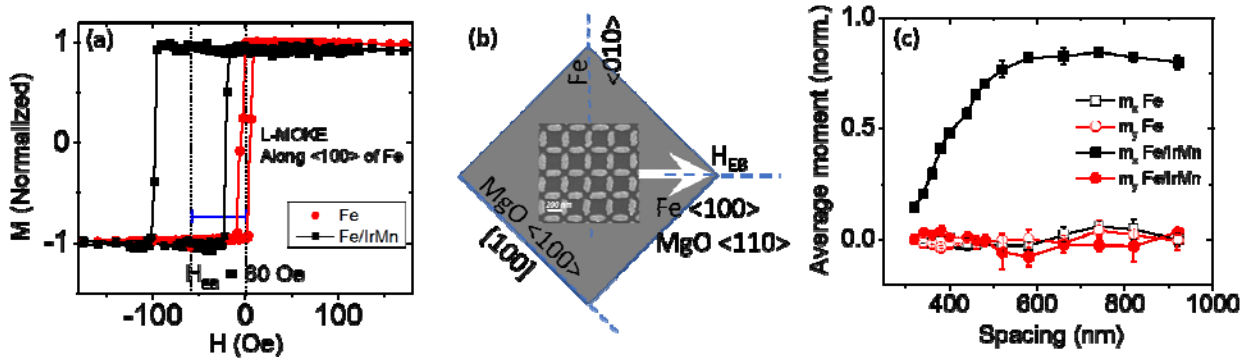

FIG. 2 a) Hysteresis of MgO/Fe(10 nm)/Pt(2 nm) and MgO/Fe(10 nm)/IrMn(8 nm)/Pt(2 nm) obtained by longitudinal magneto-optic Kerr effect measurements. The exchange-biased Fe/IrMn system has increased coercivity with a shift of 60 Oe. b) Schematic of the MgO substrate showing the crystallographic directions and direction of exchange bias, H_{EB}, of the Fe/IrMn films along with the SEM image of the ASI. c) Net magnetization components m_x and m_y of normal ASI and exchange biased ASI after the rotating sample demagnetization.

In the demagnetization process (supplementary SFig.1), the ASI devices are rotated at ~900 rpm between the poles of an electromagnet. The magnetic field is initially set to a large value of 1360 Oe and is cycled in a square wave pattern with alternating polarity, with amplitude decreasing to zero at a linear ramp rate of 0.015 Oe/sec. The period of oscillation of the square wave is set to 2 sec. Overall, the process of demagnetization for each sample took ~ 25 hours (a slower demagnetization process of 50 hours changed the vertex statistics only by ~ 6%). Magnetic force microscopy (MFM) images (Asylum Research MFP3D) of the devices were obtained at zero magnetic field over a total area of 400 μm^2, spanning between 3200 to 900 elements as the spacing is increased from 320 nm to 920 nm. The MFM images (grey scale contrast) were converted to a magnetic moment matrix to extract the vertex statistics and the net magnetic moments using Python code. Fig. 3 shows the MFM images of an unbiased Fe ASI and a Fe/IrMn EB-ASI with different lattice spacing where the vertex types are identified and marked with color codes (more on MFM images in supplementary SFig. 2).

The efficiency of the rotating sample demagnetization process is verified from values of the net magnetic moments m_x and m_y of the two sublattices of the square tile lattice. In the case of Fe ASI, values of both m_x and m_y are close to zero and indicate an efficient demagnetization [Fig. 2(c)] corresponding to the formation of large T1 domains (antiferromagnetic ordering) in a normal ASI as shown in Fig. 3. The same demagnetization protocol performed on the EB-ASI system indicates a clear distinction in the observed net values of m_x and m_y [Fig. 2(c)], i.e. m_y exhibits almost zero net moment indicating an efficient demagnetization process, but the value of m_x increases and saturates as the lattice spacing is increased. For small values of lattice spacing, the magnetostatic coupling is strong enough (small value of $H_{EB}/H_{dip} < 1$) to give rise to large T1 domains with characteristic antiferromagnet-like ordering (Fig. 3), accompanied by small values of the resultant net magnetic moment ($m_x \sim 0.15$ and $m_y \sim 0$). However, as the array spacing

increases the magnetostatic coupling decreases (H_{EB}/H_{dip} increases) and the m_x components increases and saturates, indicating the effect of local exchange bias along the +x-direction. The saturation value of m_x is close to 0.8 at larger values of H_{EB}/H_{dip}.

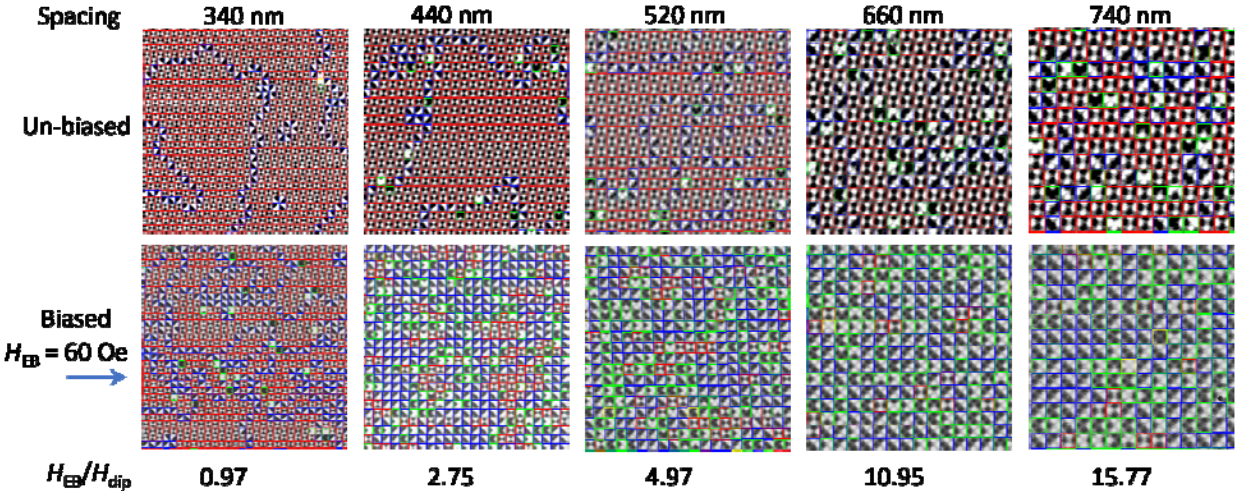

FIG. 3 Magnetic force microscopy images of a 10 μm x 10 μm area of the Fe (ASI) and Fe/IrMn (EB-ASI) array with different lattice spacings. Different types of vertices namely T1, T2, T3 and T4 are sorted and color-coded in red, blue, green and yellow square boxes respectively. To ensure good statistics four such images of 10 μm x10 μm were averaged for each lattice spacing and the errors are calculated from their standard deviation.

Fig. 4 illustrates the population statistics of different vertices as the lattice spacing is increased in (a) ASI, and (b) EB-ASI. For ASI, the predominant contribution towards the total energy of the system is only the magnetostatic interactions between the elements. This is minimized during the demagnetization process by arranging the magnetic moments to form T1 (T10 and T11) vertices (with antiferromagnetic order). Thus, for the smallest lattice spacing large areas of T1 domains, which constitute ~ 90% of the total vertices [Fig. 4(a)], can be observed. These domains are separated by "domain walls" composed of T2 (T20-T23) vertices (~9 %) with a small number of T3 (T30-T37) excitations (~1%). As the lattice spacing is increased, the population of T1 declined linearly; at the same time T2 and T3 populations increase commensurate with a decrease in T1 domain sizes. The variation in population, as a function of lattice spacing, for all four T2 vertices are identical and is the same for all eight T3 vertices. At the largest spacing of 920 nm, populations of T1, T2 and T3 become roughly equal (~30%). Even at this lattice spacing we did not observe the random distribution (12.5%, 25%, 50% and 12.5% for T1, T2, T3 and T4 respectively) indicating that it is still an interacting system. In contrast, the EB-ASI exhibits dramatically new statistics [Fig. 4(b)]. Here, at the smallest lattice spacing of 320 nm, T1 vertices constitute ~80% of the total number corresponding to the antiferromagnetic order. T2 vertices (~19%) serve as the walls separating T1 domains, and the rest (~1%) are observed as T3 excitations. Here the domain walls are mainly constituted by T20 and T21 vertices, unlike all four T2 configurations observed in ASI. With increase in lattice spacing, the population of T1 decreased steeply with a corresponding increase in population of T20, T21, T30 and T31, all of which show a trend towards saturation at larger spacing. At a spacing of 400 nm (at H_{EB}/H_{dip} ~ 1.92) a cross over in population of T10-T11 and T20-T21 is observed, and at 460 nm (H_{EB}/H_{dip} ~ 3.24) the T30-T31 population exceeds that of T1. At larger spacing one can observe a decrease in size of T10-T11 domains and at the same time the T20-

T21 domain walls expand into larger domains. Thus, a non-linear variation in population is observed unlike the normal ASI where a linear dependence of vertex populations is observed with lattice spacing. In EB-ASI as the lattice spacing is increased a mixture of ferromagnetic and antiferromagnetic domains are observed (at H_{EB}/H_{dip} ~ 1.92) with large densities of charged T30-T31 excitations. The T20-T21 and T30-T31 states have net magnetic moment aligned to the exchange bias direction. Thus, in EB-ASI the simple 4 level system of vertices, applicable to ASI, cannot be used to explain the observed statistics and microstates. The introduction of exchange bias lifts the degeneracy associated with the spin reversal symmetry of the ASI and hence there is rearrangement of energies of different vertex configurations.

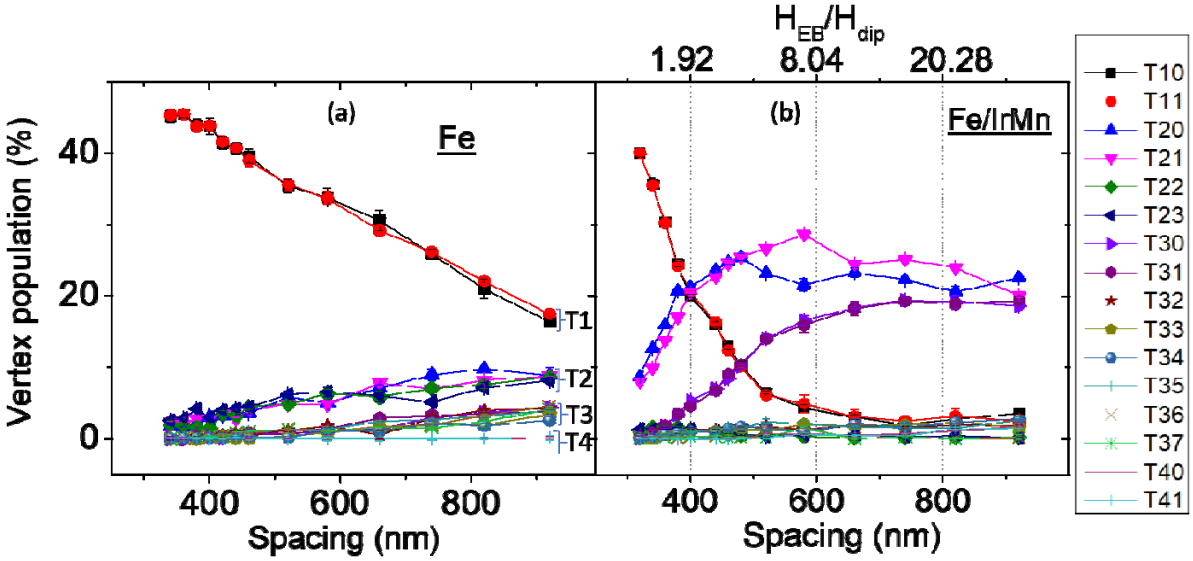

FIG. 4 Statistics of 16 different vertex types in a) ASI and b) EB-ASI plotted as a function of lattice constant. The ASI exhibits almost linear variation in populations of various vertices whereas EB-ASI indicates a highly nonlinear behavior. For the EB-ASI the top x-scale indicates the ratio of exchange bias to dipolar field (calculated values) at different lattice spacings.

The total energies of all the 16 vertices are calculated separately for different lattice spacings at different values of exchange bias from 0 to 100 Oe using micromagnetic simulation software, OOMMF [47]. The exchange bias is introduced in micromagnetic simulations as an additional Zeeman energy term due to a local magnetic field. The variation in total energy of vertices, calculated as a function of lattice spacing at H_{EB} = 0 Oe, 20 Oe and 60 Oe are shown in supplementary SFig. 4. With H_{EB} = 0, the resulting arrangement of energy levels (T1<T2<T3<T4) illustrated in Fig. 1 is maintained, with decreasing energy difference between levels, even at large lattice spacing. For EB-ASI, at H_{EB} = 20 Oe, as the lattice spacing is increased a crossover of energy of T20-T21 and T10-T11 is predicted at ~ 420 nm, in close agreement with experiment [Fig. 4(b)]. Similarly, the energy crossover of T30-T31 and T10-T11, at ~500 nm, is predicted by the simulation and experimentally observed. Thus, the experimentally measured vertex population is clearly indicative of energy level rearrangement and by comparing the observed cross-overs spacing with micromagnetic simulations, we can estimate the value of local exchange bias in the heterostructures if they were to differ from that of the bilayer film as suggested in previous reports [48,49]. In this manner, the effective exchange bias (local field) is determined to be smaller (20 Oe) compared to the value (60 Oe)

measured for the unpatterned bilayer films. The rearrangement of the vertices in an EB-ASI at large value of H_{EB}/H_{dip} >>1 is as shown Fig 1; thus, the four-level system of ASI evolves into a seven-level EB-ASI system. In the latter, the lowest energy level is composed of (T20, T21), with (T30, T31) being the first excited state. The energies of vertices with no net magnetic moment along the exchange bias direction, namely T10, T11, T32, T33, T34, T35, T40 and T41, follow their counterparts in the ASI without the local bias field. In other words, the rearrangement in energy levels happens only for those vertices (T20, T21, T22, T23, T30, T31, T36 and T37 indicated in Fig. 1) with net magnetic moment aligned such that they can couple with the local bias field.

In the EB-ASI, at a lattice spacing of ~ 400 nm, the populations of T10, T11, T20 and T21 vertices become identical and the simulations indicate that their energies are nearly equal. This scenario is similar to the extensive degeneracy (six-fold degenerate ground state composed of T10, T11, T20, T21, T22, T23) observed by Perrin *et.al* [21] on three dimensional shifted ASI with variable interaction strengths of perpendicularly and collinearly aligned moments. However, in our EB-ASI, the introduction of a Zeeman energy term arising from the local field leads only to a partial recovery of extensive degeneracy, which is four-fold (T10, T11, T20, T21) degenerate. Thus, a new ground state is obtained composed of these four vertices with the first excited state composed of type T30 and T31 vertices.

In conclusion, a new artificially engineered interacting system of exchange biased nanomagnets (EB-ASI) is demonstrated. Tuning H_{EB}/H_{dip}, by varying the EB-ASI lattice spacing, led to the observation of different ground states configurations, ranging from antiferromagnetic ordering (small H_{EB}/H_{dip}) to a mixture of antiferromagnetic and ferromagnetic order (intermediate H_{EB}/H_{dip}) and finally, to ferromagnetic order for large values of H_{EB}/H_{dip}. The introduction of a local exchange bias field makes it possible to explore different regions of configurational phase space, where the ground state configuration can be tuned by varying H_{EB}/H_{dip}. Finally, this heterostructured EB-ASI readily lends itself to a second level lithography process to further engineering the local field on the mesoscale with the bias applied only at specific sites in the lattice. Then it can be used to study the effect of pinning centers, defects/disorder on the ground state configurations (similar to work done by Drisko *et al.* [18]). It can also be a model system to compare with thermally driven spin ice subjected to an external magnetic field (similar work was carried out by Sklenar *et.al* as a part of their study on quadrupole ASI system [50]). EB-ASI might also pave the way to studies of spin fragmentation and monopole crystallization [51] which were previously observed in spin ices [52,53] and artificial kagome spin ice systems [54]. Such work is in progress.

This work was supported by the National Science Foundation grant, NSF/DMR 1604186. Part of this work was conducted at the Washington Nanofabrication Facility / Molecular Analysis Facility, a National Nanotechnology Coordinated Infrastructure (NNCI) site at the University of Washington, which is supported in part by funds from the Molecular Engineering & Sciences Institute, the Clean Energy Institute, the Washington Research Foundation, the M. J. Murdock Charitable Trust, the National Science Foundation and the National Institutes of Health.

---

[1] R. F. Wang, C. Nisoli, R. S. Freitas, J. Li, W. Mcconville, B. J. Cooley, M. S. Lund, N. Samarth, C. Leighton, V. H. Crespi, and P. Schiffer, Nature **439**, 303 (2006).

[2] R. Moessner and A. P. Ramirez, Phys. Today **59**, 24 (2006).

[3] C. Nisoli, R. Moessner, and P. Schiffer, Rev. Mod. Phys. **85**, 1473 (2013).

[4] S. T. Bramwell and M. J. P. Gingras, Science **294**, 1495 (2001).
[5] M. Harris, S. Bramwell, D. McMorrow, T. Zeiske, and K. W. Godfrey, Phys. Rev. Lett. **79**, 2554 (1997).
[6] L. F. Cugliandolo, J. Stat. Phys. **167**, 499 (2017).
[7] M. J. Morrison, T. R. Nelson, and C. Nisoli, New J. Phys. **15**, 045009 (2013).
[8] D. Levis, Two-Dimensional Spin Ice and the Sixteen-Vertex Model, Ph.D. Thesis, Université Pierre et Marie Curie, Paris, France, 2012.
[9] I. Gilbert, C. Nisoli, and P. Schiffer, Phys. Today **69**, 55 (2017).
[10] J. Cumings, L. J. Heyderman, C. H. Marrows, and R. L. Stamps, New J. Phys. **16**, 075016 (2014).
[11] L. J. Heyderman and R. L. Stamps, J. Phys. Condens. Matter **25**, 363201 (2013).
[12] I. Gilbert, Y. Lao, I. Carrasquillo, L. O'brien, J. D. Watts, M. Manno, C. Leighton, A. Scholl, C. Nisoli, and P. Schiffer, Nat. Phys. **12**, 162 (2016).
[13] E. Mengotti, L. J. Heyderman, A. F. Rodríguez, F. Nolting, R. V Hügli, and H. Braun, Nat. Phys. **7**, 68 (2011).
[14] S. Gliga, G. Hrkac, C. Donnelly, J. Büchi, A. Kleibert, J. Cui, A. Farhan, E. Kirk, R. V Chopdekar, Y. Masaki, N. S. Bingham, A. Scholl, R. L. Stamps, and L. J. Heyderman, Nat. Mater. **16**, 1106 (2017).
[15] I. Gilbert, G. W. Chern, S. Zhang, L. O'Brien, B. Fore, C. Nisoli, and P. Schiffer, Nat. Phys. **10**, 670 (2014).
[16] S. Zhang, I. Gilbert, C. Nisoli, G. Chern, M. J. Erickson, L. O. Brien, C. Leighton, P. E. Lammert, V. H. Crespi, and P. Schiffer, Nature **500**, 553 (2013).
[17] D. Shi, Z. Budrikis, A. Stein, S. A. Morley, P. D. Olmsted, G. Burnell, and C. H. Marrows, Nat. Phys. **14**, 309 (2018).
[18] J. Drisko, T. Marsh, and J. Cumings, Nat. Commun. **8**, 14009 (2017).
[19] R. Wang, Geometrical Magnetic Frustration and Demagnetization of Artificial Spin Ice, Ph.D. Thesis, Pennsylvania State University, 2007.
[20] R. Moessner and G. Mo, Phys. Rev. Lett. **96**, 237202 (2006).
[21] Y. Perrin, B. Canals, and N. Rougemaille, Nature **540**, 410 (2016).
[22] Y. Qi, T. Brintlinger, and J. Cumings, Phys. Rev. B **77**, 094418 (2008).
[23] Yi Qi, Artificial Kagome Spin Ice, Ph.D. Thesis, University of Maryland, College Park, 2008.
[24] P. E. Lammert, X. Ke, J. Li, C. Nisoli, D. M. Garand, V. H. Crespi, and P. Schiffer, Nat. Phys. **6**, 786 (2010).
[25] C. Nisoli, R. Wang, J. Li, W. F. Mcconville, P. E. Lammert, P. Schiffer, and V. H. Crespi, Phys. Rev. Lett. **98**, 217203 (2007).
[26] C. Nisoli, J. Li, X. Ke, D. Garand, P. Schiffer, and V. H. Crespi, Phys. Rev. Lett. **105**, 047205 (2010).
[27] R. C. Silva and R. J. C. Lopes, Phys. Rev. B **87**, 014414 (2013).
[28] R. F. Wang, J. Li, W. Mcconville, C. Nisoli, X. Ke, J. W. Freeland, V. Rose, M. Grimsditch, P. Lammert, V. H. Crespi, and P. Schiffer, J. Appl. Phys. **101**, 09J104 (2014).
[29] J. P. Morgan, A. Bellew, A. Stein, S. Langridge, and C. H. Marrows, Front. Phys. **1**, 28 (2013).
[30] X. Ke, J. Li, C. Nisoli, P. E. Lammert, W. Mcconville, R. F. Wang, V. H. Crespi, and P. Schiffer, Phys. Rev. Lett. **101**, 037205 (2008).
[31] J. M. Porro, A. Bedoya-Pinto, A. Berger, and P. Vavassori, New J. Phys. **15**, 055012

(2013).
[32] A. Farhan, P. M. Derlet, A. Kleibert, A. Balan, R. V Chopdekar, M. Wyss, J. Perron, A. Scholl, F. Nolting, and L. J. Heyderman, Phys. Rev. Lett. **111**, 057204 (2013).
[33] J. P. Morgan, A. Stein, S. Langridge, and C. H. Marrows, Nat. Phys. **7**, 75 (2011).
[34] A. Farhan, A. Kleibert, P. M. Derlet, L. Anghinolfi, A. Balan, R. V. Chopdekar, M. Wyss, S. Gliga, F. Nolting, and L. J. Heyderman, Phys. Rev. B **89**, 214405 (2014).
[35] A. Farhan, P. M. Derlet, L. Anghinolfi, A. Kleibert, and L. J. Heyderman, Phys. Rev. B **96**, 064409 (2017).
[36] L. Anghinolfi, H. Luetkens, J. Perron, M. G. Flokstra, O. Sendetskyi, A. Suter, T. Prokscha, P. M. Derlet, S. L. Lee, and L. J. Heyderman, Nat. Commun. **6**, 1 (2015).
[37] J. Park, B. L. Le, J. Sklenar, G. Chern, J. D. Watts, and P. Schiffer, Phys. Rev. B **96**, 024436 (2017).
[38] Y. Lao, F. Caravelli, M. Sheikh, J. Sklenar, D. Gardeazabal, J. D. Watts, A. M. Albrecht, A. Scholl, K. Dahmen, C. Nisoli, and P. Schiffer, Nat. Phys. **14**, 723 (2018).
[39] W. Zhang and K. M. Krishnan, Mater. Sci. Eng. R **105**, 1 (2016).
[40] J. Nogués and I. K. Schuller, J. Magn. Magn. Mater. **192**, 203 (1999).
[41] A. E. Berkowitz and K. Takano, J. Magn. Magn. Mater. **200**, 552 (1999).
[42] R. L. Stamps, J. Phys. D. Appl. Phys. **33**, R247 (2000).
[43] W. Zhang, Competing Anisotropies in Epitaxial Exchange Biased Thin Films and Patterned Nanostructures, Ph.D. Thesis, University of Washington, 2013.
[44] W. Zhang and K. M. Krishnan, J. Magn. Magn. Mater. **324**, 3129 (2012).
[45] W. Zhang, M. E. Bowden, and K. M. Krishnan, Appl. Phys. Lett. **98**, 092503 (2011).
[46] V. Kapaklis, U. B. Arnalds, A. Harman-Clarke, E. T. Papaioannou, M. Karimipour, P. Korelis, A. Taroni, P. C. W. Holdsworth, S. T. Bramwell, and B. Hjorvarsson, New J. Phys. **14**, 035009 (2012).
[47] M. Donahue and D. Porter, OOMMF User's Guid. Version 1.0, Interag. Rep. NISTIR 6376, NIST, Gaithersburg, MD (1999).
[48] J. Nogués, J. Sort, V. Langlais, V. Skumryev, S. Suriñach, J. S. Muñoz, and M. D. Baró, Phys. Rep. **422**, 65 (2005).
[49] V. Baltz, J. Sort, S. Landis, B. Rodmacq, and B. Dieny, Phys. Rev. Lett. **94**, 117201 (2005).
[50] J. Sklenar, Y. Lao, A. Albrecht, J. D. Watts, C. Nisoli, G. W. Chern, and P. Schiffer, Nat. Phys. **15**, 191 (2019).
[51] M. E. Brooks-Bartlett, S. T. Banks, L. D. C. Jaubert, A. Harman-Clarke, and P. C. W. Holdsworth, Phys. Rev. X **4**, 011007 (2014).
[52] S. Petit, E. Lhotel, B. Canals, M. Ciomaga Hatnean, J. Ollivier, H. Mutka, E. Ressouche, A. R. Wildes, M. R. Lees, and G. Balakrishnan, Nat. Phys. **12**, 746 (2016).
[53] E. Lefrançois, V. Cathelin, E. Lhotel, J. Robert, P. Lejay, C. V. Colin, B. Canals, F. Damay, J. Ollivier, B. Fåk, L. C. Chapon, R. Ballou, and V. Simonet, Nat. Commun. **8**, 209 (2017).
[54] B. Canals, I. Chioar, V. Nguyen, M. Hehn, D. Lacour, F. Montaigne, A. Locatelli, T. O. Mentes, B. S. Burgos, and N. Rougemaille, Nat. Commun. **7**, 11446 (2016).

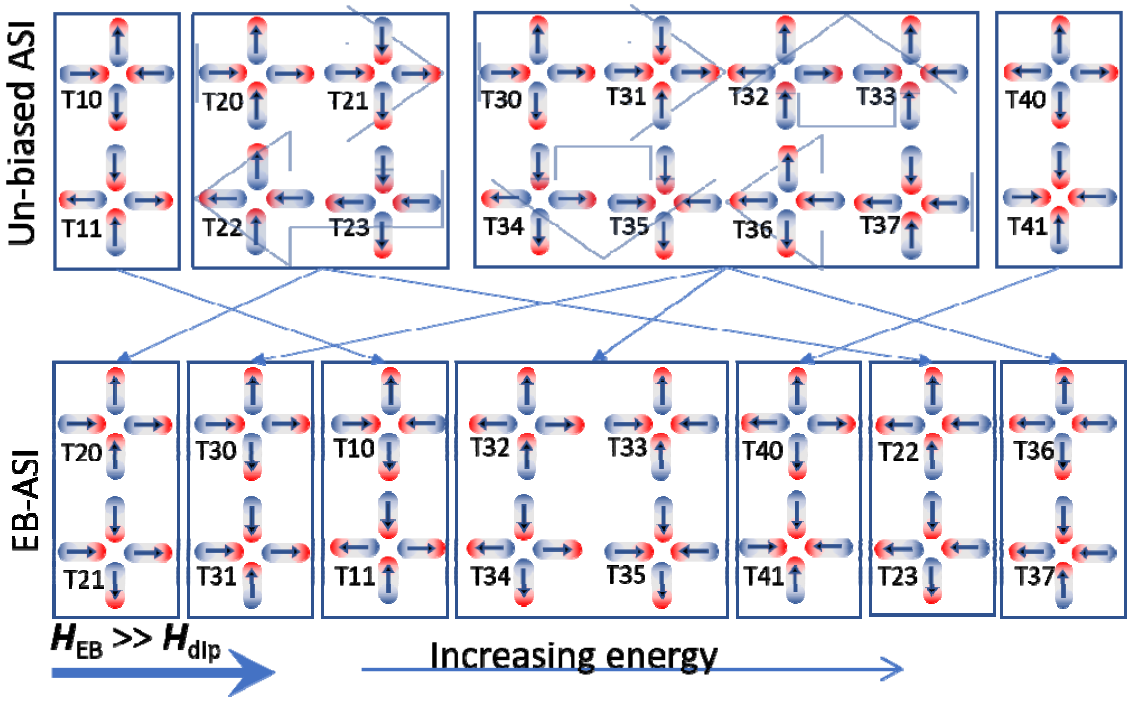

FIG. 1 *Schematic representation of the energy levels of vertices for a normal ASI. The vertices are enumerated as (T10, T11), (T20, T21, T22, T23), (T30, T31, T32, T33, T34, T35, T36, T37) and (T40, T41). (top) The four possible types of vertices are (1) the ground state, T1 (two spins out, two spins in, no net moment), which is two-fold degenerate, with the two states related by a global spin-flip. (2) A saturated state, T2 (two spins out, two spins in, with net moment), with four-fold degeneracy, and where spins have a net projection parallel or antiparallel to the* x*-axis. (3) An eight-fold degenerate configuration, T3 (one spin in, three spins out, OR, one spin out and three spins in, with moment along the x- or y-direction), and (4) a two-fold degenerate, T4 (all four spins in or all four spins out). (bottom) In the exchange biased ASI the vertices are energetically rearranged and represented here based on micromagnetic simulations. The 4-level system rearranges into a 7-level system. The dipolar vertices, with effective magnetic moments parallel to the bias direction are now lower in energy, with (T20, T21) being the ground state and (T10, T11) now excited even above the (T30, T31) states. Further, these energy levels can be tuned by the ratio* H_{EB}/H_{dip} *as described in the text.*

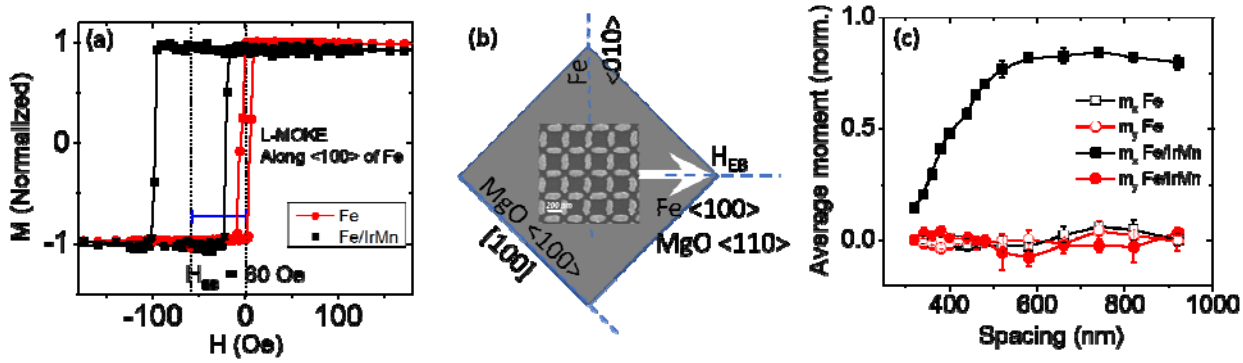

FIG. 2. a) Hysteresis of MgO/Fe(10 nm)/Pt(2 nm) and MgO/Fe(10 nm)/IrMn(8 nm)/Pt(2 nm) obtained by longitudinal magneto-optic Kerr effect measurement. The exchange-biased Fe/IrMn system has increased coercivity with a shift of 60 Oe. b) Schematic of the MgO substrate showing the crystallographic directions and direction of exchange bias, H_{EB}, of the Fe/IrMn films along with the SEM image of the ASI. c) Net magnetization components m_x and m_y of normal ASI and exchange biased ASI after the rotating sample demagnetization.

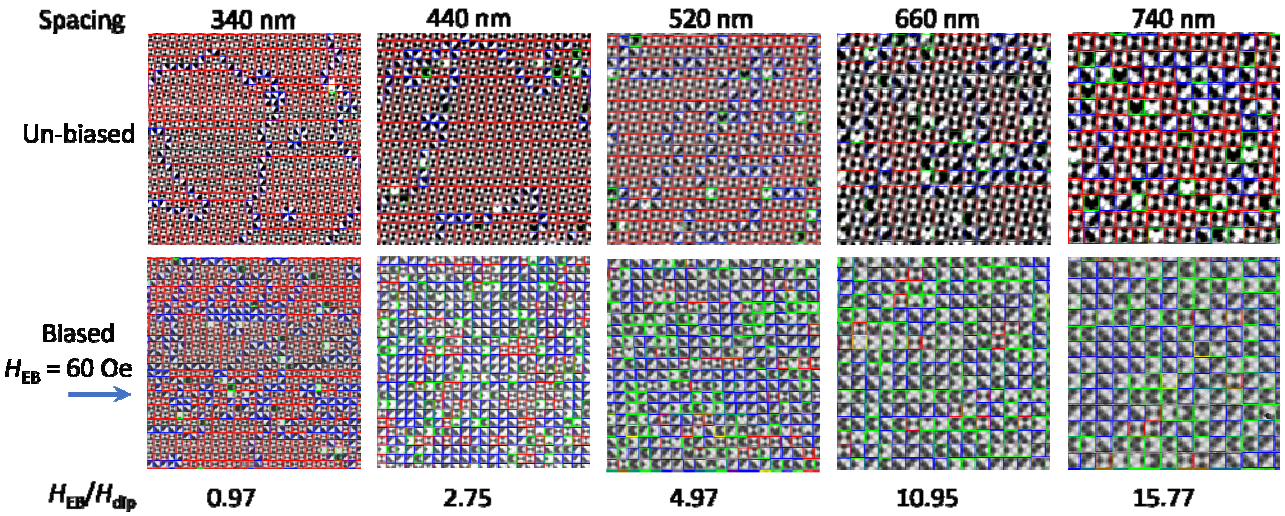

FIG. 3 Magnetic force microscopy images of a 10 μm x 10 μm area of the Fe (ASI) and Fe/IrMn (EB-ASI) array with different lattice spacings. Different types of vertices namely T1, T2, T3 and T4 are sorted and color-coded in red, blue, green and yellow square boxes respectively. To ensure good statistics four such images of 10 μm x10 μm were averaged for each lattice spacing and the errors are calculated from their standard deviation.

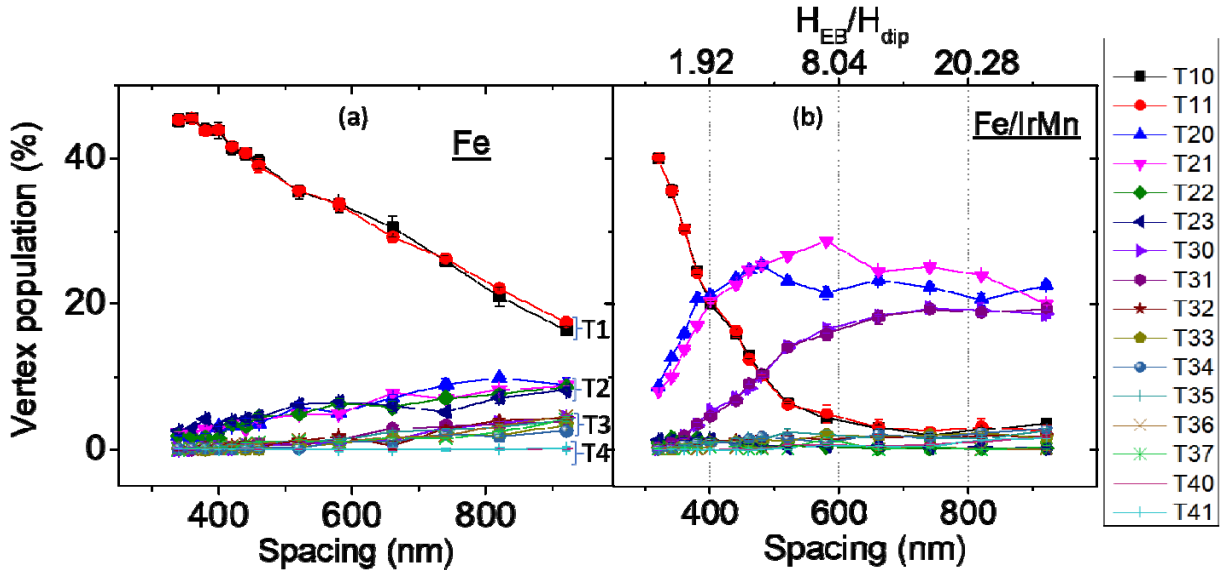

FIG. 4 Statistics of 16 different vertex types in a) ASI and b) EB-ASI plotted as a function of lattice constant. The ASI exhibits almost linear variation in populations of various vertices whereas EB-ASI indicates a highly nonlinear behavior. For the EB-ASI the top x-scale indicates the ratio of exchange bias to dipolar field (calculated values) at different lattice spacings.